

Studies of laser wakefield structures and electron acceleration in underdense plasmas^{a)}

A. Maksimchuk,^{1,b)} S. Reed,¹ S. S. Bulanov,¹ V. Chvykov,¹ G. Kalintchenko,¹ T. Matsuoka,¹ C. McGuffey,¹ G. Mourou,^{1,c)} N. Naumova,^{1,c)} J. Nees,¹ P. Rousseau,¹ V. Yanovsky,¹ K. Krushelnick,¹ N. H. Matlis,^{2,d)} S. Kalmykov,² G. Shvets,² M. C. Downer,² C. R. Vane,³ J. R. Beene,³ D. Stracener,³ and D. R. Schultz³

¹*FOCUS Center and Center for Ultrafast Optical Science, University of Michigan, Ann Arbor, Michigan 48109-2099, USA*

²*FOCUS Center, Department of Physics, University of Texas at Austin, Austin, Texas 78712-1081, USA*

³*Physics Division, Oak Ridge National Laboratory, Oak Ridge, Tennessee 37831-6372, USA*

(Received 18 November 2007; accepted 25 January 2008; published online 6 March 2008)

Experiments on electron acceleration and optical diagnostics of laser wakes were performed on the HERCULES facility in a wide range of laser and plasma parameters. Using frequency domain holography we demonstrated single shot visualization of individual plasma waves, produced by 40 TW, 30 fs laser pulses focused to the intensity of 10^{19} W/cm² onto a supersonic He gas jet with plasma densities $n_e < 10^{19}$ cm⁻³. These holographic “snapshots” capture the variation in shape of the plasma wave with distance behind the driver, and resolve wave front curvature seen previously only in simulations. High-energy quasimonoenergetic electron beams were generated using plasma density in the range $1.5 \times 10^{19} \leq n_e \leq 3.5 \times 10^{19}$ cm⁻³. These experiments demonstrated that the energy, charge, divergence, and pointing stability of the beam can be controlled by changing n_e , and that higher electron energies and more stable beams are produced for lower densities. An optimized quasimonoenergetic beam of over 300 MeV and 10 mrad angular divergence is demonstrated at a plasma density of $n_e \approx 1.5 \times 10^{19}$ cm⁻³. The resultant relativistic electron beams have been used to perform photo-fission of ²³⁸U with a record high reaction yields of $\sim 3 \times 10^5$ /J. The results of initial experiments on electron acceleration at 70 TW are discussed. © 2008 American Institute of Physics. [DOI: 10.1063/1.2856373]

I. INTRODUCTION

Laser-wakefield accelerators (LWFAs) have the potential of becoming the next generation of particle accelerators¹ because plasma as an ionized medium can support extremely high electric fields reaching several hundreds of GV/m. When an intense laser pulse interacts with an underdense plasma it excites plasma waves propagating near light speed behind the pulse. These waves are generated through the displacement of plasma electrons driven by the ponderomotive force of the laser. For sufficiently large amplitude plasma waves, electrons in the background plasma can be trapped and accelerated by the longitudinal electric fields of the waves to very high energies over very short distances.

Earlier laser wakefield experiments concentrated on the acceleration of electron beams in a self-modulated regime^{2–4} and in a forced wakefield regime.⁵ More recently quasimonoenergetic electron beams with energy of 10–170 MeV were produced^{6–11} using ultrashort laser pulses, which undergo pulse modification (self-modulation and compression)¹² to reach the resonant condition $c\tau \approx \lambda_p/2$, where τ is the laser pulse duration at FWHM, c is light

speed, and λ_p is the plasma wavelength. Guiding of the laser pulse in capillary discharge plasma allowed for electron acceleration up to 1 GeV,¹³ and the use of colliding laser pulses for controlled injection generated electron beams of 15–250 MeV.¹⁴

Despite the great recent experimental progress there are still unresolved issues. There are two groups of problems which we address and partially resolve in the present paper. First is a single-shot diagnostic (visualization) of the near-luminous accelerating structure three-dimensional (3D) wake plasma wave. The second problem is scaling and controlling the electron beam parameters with plasma density variation and application of optimized electron beams to the photo-fission reactions.

Electron beam quality parameters from LWFAs such as energy, energy spread, angular divergence, bunch charge, and its duration depend sensitively on the plasma wakefield structures. Direct visualization of these structures and their evolution is critical for understanding and controlling LWFA output. Previous direct measurements of laser wakes with spatial resolution better than a plasma wavelength λ_p (Refs. 15–18) used frequency-domain interferometry,¹⁹ in which a focused femtosecond probe pulse measured local electron density at only a single time delay behind the driving pulse within the copropagating wake for each laser shot. Wake structure was then accumulated thoroughly by probing the plasma at different delay at each subsequent shot. The multishot diagnostic thus averaged over substantial shot-to-shot

^{a)}Paper K12 1, Bull. Am. Phys. Soc. 52, 183 (2007).

^{b)}Invited speaker. Electronic mail: tolya@umich.edu.

^{c)}Present address: Laboratoire d'Optique Appliquée, Ecole Polytechnique, ENSTA, 91761 Palaiseau, France.

^{d)}Present address: Lawrence Berkeley National Laboratory, Berkeley, California 94720.

variations of the plasma structure and did not provide for rapid feedback for scanning and optimization of experimental parameters. We meet this challenge by recording two-dimensional features of the plasma wave in a single shot using frequency-domain holography (FDH).²⁰ These measurements make the subject of Sec. II A. The holographic “snapshots” record multiple wake periods of the mildly nonlinear nonbroken plasma wake and capture the buildup of the wave front curvature with the distance behind the driver; the features previously seen only in the simulations. We have implemented the FDH in plasmas with electron density $n_e < 10^{19} \text{ cm}^{-3}$ where no self-trapping of electrons from the background occurs.²¹ For higher electron densities the electron self-injection did occur and we observed quasimonoenergetic electron beams with energy above 80 MeV.

The role of electron plasma density as a parameter governing the peak energy and quality of electron beam from the LWFA recently became a matter of discussion.^{6,11,22–24} Moreover it is also important to know electron energy scaling with plasma density for future Petawatt experiments with gas targets, which have the potential to produce energies in excess of GeV.^{23–26} In Sec. II B, we report the results of our systematic experimental study of the plasma density effect on the electron beam quality.²⁷ We demonstrate that the electron beam energy, charge, divergence, and pointing stability vary widely but reproducibly within a specific density range. We show that scaling and tunability of electron energy as a function of n_e is consistent with the dephasing of accelerated electrons from the plasma wave and demonstrate the generation of quasimonoenergetic electrons with optimized energy of $320 \pm 50 \text{ MeV}$, twice higher for a self-guided LWFA than reported in the ^{6,22} divergence of 10 mrad and rms pointing stability of 7 mrad. In Sec. II C we describe the experiment in which pulses of nearly monoenergetic high-energy electrons were converted into high-energy bremsstrahlung to perform photofission in depleted uranium.^{28,29} Quantitative γ -ray spectroscopy of the irradiated uranium sample indicates that a record high yield of 3×10^5 reactions were produced per Joule of laser energy. In Sec. II D we present the results of the initial experiments on electron acceleration at a laser power of 70 TW.

II. EXPERIMENTS AND DISCUSSION

A. Snapshots of laser-generated wakefields

Experiments were performed on the Ti:Sapphire HERCULES laser system at the Center for Ultrafast Optical Science of the University of Michigan³⁰ which delivers 40 TW, 800 nm, 30 fs pulses to the target. The uncompressed beam is split 90-10 into pump and probe beams, which are independently compressed. The pump is focused with an $f/13$ ($f=1 \text{ m}$) parabola onto a supersonic 2 mm He gas jet providing a peak intensity up to $I_0=10^{19} \text{ W/cm}^2$. The corresponding dimensionless electric field amplitude $a_0=8.5 \times 10^{-10} \lambda_0(\mu\text{m}) I_0^{1/2} (\text{W cm}^{-2})=2.2$. The Rayleigh range of the interaction is $Z_R=\pi d_0^2/(2\lambda_0 \ln 2) \approx 1 \text{ mm}$, where $d_0=18 \mu\text{m}$ is the focal spot diameter at FWHM. The focused pulse ionizes the gas and creates a near-luminous plasma wakefield trailing the pulse. At densities below 10^{19} cm^{-3} the

plasma wave remained nonbroken (no fast electrons detected) and multiple wake periods behind the driver were captured in a single shot with FDH, a technique designed to image structures propagating near the speed of light c . FDH uses a long, wide probe pulse that illuminates the entire plasma perturbations like the “object” beam in conventional holography. Interference of this probe with an equally extended “reference” pulse on a detector encodes the object’s phase structure, which is subsequently “read” to reconstruct the object, completing the analogy with conventional holography. In the probe line, two second-harmonic pulses are generated: First, the input fundamental is up-converted to 400 nm in a thin (200 μm) KDP crystal; the remaining, nearly undepleted 800 and the 400 nm pulses then pass through a half-inch of glass, causing them to separate temporally via group-velocity dispersion (GVD); a second thin KDP crystal generates a second 400 nm pulse perfectly collinear with the first, and advanced in time by $\sim 3 \text{ ps}$. The probe pulses are recombined collinearly with the pump through a one inch thick high reflector for 800 nm with high transmission at 400 nm. This recombining optic stretches the probe pulses to $\sim 1 \text{ ps}$ via linear dispersion, establishing the temporal window for FDH. The temporally advanced 2ω pulse is timed to arrive before the pump at the jet, where it acts as a reference pulse for FDH. The second 2ω pulse rides with the pump and the plasma disturbances (ionization front and wakefield), which impart a time/frequency-dependent phase shift to the probe pulse. This shift is recovered by interfering the probe and the reference in a spectrometer. Imaging optics relay the interaction plane to the spectrometer slit with a threefold magnification, and provide a spatial resolution of several microns.

The FD hologram was analyzed by reconstructing the probe’s electric field $E_{pr}(r, \omega) = |E(r, \omega)| e^{i\phi(r, \omega)}$, where $\phi(r, \omega) = \phi_{\text{chirp}}(r, \omega) + \delta\phi_{pr}(r, \omega)$ in the spectral domain, than Fourier-transforming to the time-domain to recover the temporal phase perturbation $\delta\phi_{pr}(r, \xi)$ from which the wake electron density $n_e(r, \xi)$ is derived using the relation $\delta\phi_{pr}(r, \xi) \approx e^2 \lambda_{pr} L n_e(r, \xi) / \gamma(r, \xi) m c^2$ for uniform plasma with length L . Here $\gamma = (1 - v^2/c^2)^{1/2}$ is a relativistic Lorentz factor, and e , m , and v are the electron charge, rest mass, and oscillation velocity, respectively. Chirp phase $\phi_{\text{chirp}}(r, \omega)$ from the linear dispersion in the recombining optics is measured independently. The probe amplitude $|E(r, \omega)|$ modulated by the wake is also recovered from the hologram. A LabVIEW based analysis program running on a personal computer was used to integrate the process of data acquisition, reconstruction, and display of the wake density structure within a few seconds after the shot.

Figure 1(a) shows the ionization front and wake produced by an $\sim 30 \text{ TW}$ laser pulse. This wake has curved wave fronts, a clear signature of strongly driven, nonlinear laser–plasma interaction.^{31–33} The wave fronts evolve from flat profiles immediately behind the pump to curved “horseshoe” profiles after several periods. A wakefield produced by a 35 TW pump focused to $1/e^2$ intensity radius $r_0=25 \mu\text{m}$, simulated in particle-in-cell (PIC) code WAKE (Ref. 34) and shown in Fig. 1(b), best reproduces the wave front curvature buildup with a distance behind the driving pulse, the relative

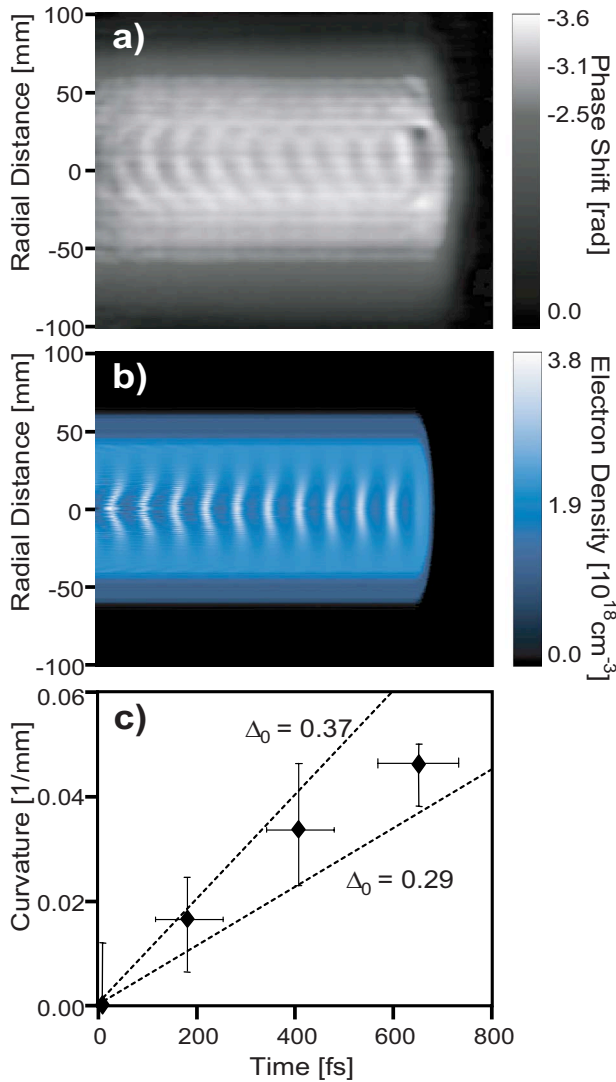


FIG. 1. (Color online) (a) Reconstructed phase profile $\delta\phi_{pr}(r, \zeta)$ for an ~ 30 TW pump, $n_e = 2.2 \times 10^{18} \text{ cm}^{-3}$. (b) Simulated density profile $n_e(r, \zeta)$. (c) Evolution of the reciprocal radius of wave front curvature behind the pump (data points), compared with calculated evolution (dashed lines) for indicated wake potential amplitudes. Each data point (except at $\zeta=0$) averages over three adjacent periods. The horizontal error bars extend over the three periods averaged, and the vertical error bars extend over the range of fitted curvature values averaged.

widths of the wake and the regions He ionization. The data points plotted in Fig. 1(c) show the evolution of the reciprocal wave front radius $\rho^{-1}(\zeta)$, obtained by fitting the wave fronts within $r < r_0$ to circular arcs.^{21,35} Such curvature, though simulated with nonlinear fluid³² and particle^{31,33} codes, has never previously been observed in the laboratory.

The wave front curves because as the plasma wave amplitude $\delta_0 \equiv |\delta n_e(r=0)/n_e|_{\text{max}}$ approaches unity on the axis, the electrons making up the wave oscillate relativistically ($\gamma > 1$), causing $\omega_p(r=0)$ to decrease by $\sqrt{\gamma}$ relative to its off-axis value.^{31,32} Thus, $\rho^{-1}(\zeta)$ depends sensitively on δ_0 ; for weakly relativistic ($\gamma \lesssim 2$) wakes, simulations are consistent with the analytic approximation³⁵ $\rho^{-1}(\zeta) \approx 0.45 \zeta [\Delta_0/r_0]^2$, with ρ and r_0 in micrometers and ζ in femtoseconds. Here Δ_0 is the amplitude of oscillations in the electrostatic wake potential (normalized to mc^2/e), from

which δ_0 is determined exactly ($\delta_0 \rightarrow \Delta_0$ for small δ_0).³² FDH measurement of $\rho(\zeta)$ thus determines the peak amplitude of the nonlinear wake. This is illustrated by the theoretical curves in Fig. 1(c), showing simulated $\rho^{-1}(\zeta)$ for $\Delta_0 = 0.29$ and 0.37 , $r_0 = 25 \text{ } \mu\text{m}$, which bound the experimental values. $\Delta_0 = 0.33 \pm 0.04$ (hence $\delta_0 \approx 0.5$) is thus consistent with the data. The curvature is important for collimation of injected and accelerated electrons.^{32,35} It also underlies electron self-injection^{6–8} and transverse wave breaking.^{31,33} Extension of the FDH diagnostics to the regimes with broken wakes (higher density/laser intensity) is a subject of our ongoing work.

In the experiments described here, the maximum density at which wakefields were recovered was $6 \times 10^{18} \text{ cm}^{-3}$. This limitation is not intrinsic to FDH, but rather was set by two accompanying phenomena: (i) Contamination of the signal with continuum generated by the drive laser which increases dramatically at higher densities, and (ii) group velocity walk-off between the probe pulse at 400 nm and the wake structure which propagates at the group velocity of the drive laser at 800 nm. Continuum generation by the drive pulse is due in large part to ionization-induced blue-shifting of the pulse at the ionization front, and can extend from the fundamental frequency down past the second harmonic, causing it to coherently interfere with the probe pulses and generate artifacts in the reconstructed signal. This noise source could potentially be avoided by preionizing the plasma. The group velocity walk-off between the pump and the probe are due to differing indices of refraction for the plasma at 400 nm and 800 nm. As a result, the structure being recorded on the probe pulse is shifting during the integration time of the interaction, causing the signal to be washed out. The amount of walk-off increases with electron density and can be estimated as $\Delta t_{\text{walk-off}} = L_{pl}/v_g(800 \text{ nm}) - L_{pl}/v_g(400 \text{ nm})$, where $v_g = c[1 - (\omega_p/\omega)^2]^{1/2}$ is the group velocity in plasma, and L_p is the plasma length. In order to be able to resolve the wake structure, the amount of walk-off must be less than one plasma period. For an interaction distance of 2 mm, the walk-off between 400 nm light and 800 nm light is about 10% of the plasma period at $\sim 2 \times 10^{18} \text{ cm}^{-3}$, but becomes equal to the plasma period at a density of $\sim 2 \times 10^{19} \text{ cm}^{-3}$. In order to overcome this limit, it is thus necessary to either decrease the interaction distance, or decrease the wavelength difference between the drive beam and the probe beam. Since the intensity of continuum light becomes much higher near the wavelength of the drive laser, it is necessary to solve both limitations at once.

B. Quasimonoenergetic electron generation

We have studied electron acceleration for the laser power of 40 TW, focusing geometry described in Sec. II and for plasma density in the range $1 \times 10^{19} \leq n_e \leq 5 \times 10^{19} \text{ cm}^{-3}$. The electron beam's spatial distribution was measured using a LANEX phosphor screen imaged onto a 12-bit cooled Charge-Coupled Device (CCD). The electron energy spectrum was measured using a dipole magnetic spectrometer with detection on a LANEX screen. The dynamics of the laser-plasma interaction was monitored *in situ*

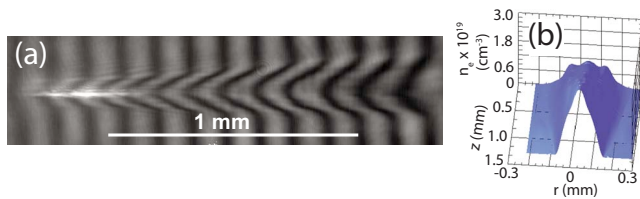


FIG. 2. (Color online) (a) Interferogram of high-intensity laser-gas jet target interaction for the delay of 10 ps. (b) The reconstructed spatial distribution of the electron density. The backing pressure of the nozzle was 45 psi and the reconstructed electron density on-axis is $n_e = (2.2 \pm 0.2) \times 10^{19} \text{ cm}^{-3}$.

using a modified Mach–Zehnder interferometer with a variable delay line. Typical interferogram taken at a 10 ps delay relative to the arrival of the main pulse and electron density reconstruction using Abel inversion are presented in Fig. 2.

An electron beam with divergence $\sim 10 \text{ mrad}$ was generated using plasma electron densities between 1.5×10^{19} and $3 \times 10^{19} \text{ cm}^{-3}$ (Fig. 3(a)). Higher plasma densities lead to larger diameter electron beams (Fig. 3(b)) and even to the beam break up. For electron densities below $1.5 \times 10^{19} \text{ cm}^{-3}$ no fast electrons were detected. The pointing stability of the electron beam strongly depended on plasma electron density as well (Fig. 3(c)). It was found that the lower densities result in more directional electron beams. At densities of 1.5×10^{19} to $1.8 \times 10^{19} \text{ cm}^{-3}$, the rms of electron beam pointing stability was only 0.46° which is approximately one-tenth of the laser beam cone. On the other hand,

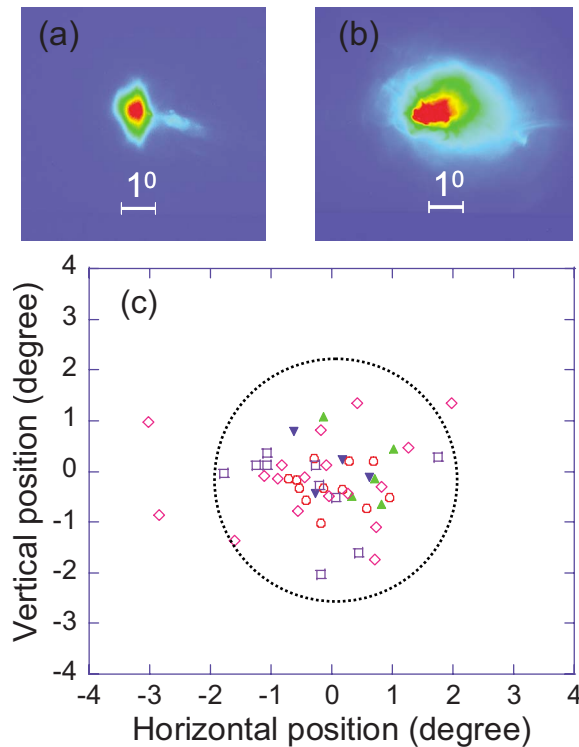


FIG. 3. (Color online) Images of the electron beam on the LANEX screen for electron density of (a) $2 \times 10^{19} \text{ cm}^{-3}$ and (b) $3.5 \times 10^{19} \text{ cm}^{-3}$. (c) Beam pointing stability for electron density ranging from 1.5×10^{19} to $3.5 \times 10^{19} \text{ cm}^{-3}$. Symbols correspond to electron density: (▼) $1.5 \times 10^{19} \text{ cm}^{-3}$, (▲) $1.8 \times 10^{19} \text{ cm}^{-3}$, (◇) $2 \times 10^{19} \text{ cm}^{-3}$, (□) $3 \times 10^{19} \text{ cm}^{-3}$, and (○) $3.5 \times 10^{19} \text{ cm}^{-3}$. The large dotted circle indicates the size of the laser beam on a phosphor screen. The laser cone angle is 4.3° .

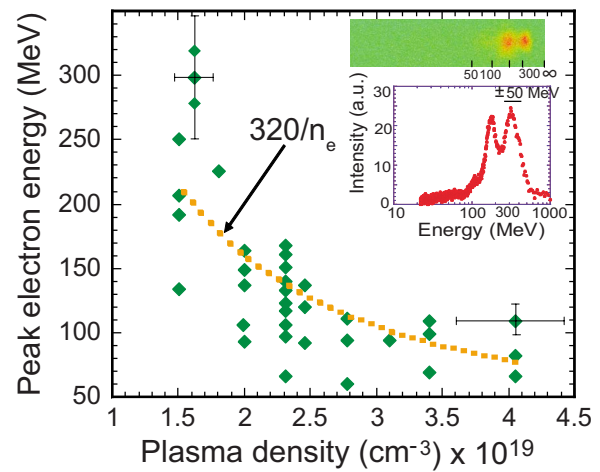


FIG. 4. (Color online) The dependence of the maximum electron energy vs plasma density. The dotted line is the $1/n_e$ fit. The inset shows measured electron spectrum and lineout for plasma density $n_e = 1.5 \times 10^{19} \text{ cm}^{-3}$ exhibiting a double peak structure with maximum energy of $320 \pm 50 \text{ MeV}$.

an analysis of light transmitted through the plasma, which was measured simultaneously with electron beam imaging, showed high laser-beam stability with shot-to-shot angular variations 100 times less than the electron beam pointing stability, suggesting it is not the laser but plasma accelerating structures are the main source of electron beam angular fluctuations. The laser beam energy losses in the plasma were in the range 65%–90% and larger for higher densities. The electron beam charge measured by the integrating current transformer (ICT) decreased from 0.5 nC to 0.3 nC as the density was reduced from $4 \times 10^{19} \text{ cm}^{-3}$ to 3×10^{19} , and below $2 \times 10^{19} \text{ cm}^{-3}$ the beam charge dropped by approximately two orders of magnitude.

Electron beam spectroscopy was performed using a dipole magnet with $B = 0.26 \text{ T}$. We placed in front of the dipole a 0.8-mm wide slit made out of two 10 mm thick lead blocks. The angular width of the slit was 5 mrad, two times smaller than the narrowest electron beam observed in the experiment. This setup allowed for an improved spectral resolution in the electron momentum measurements in contrast to whole beam spectroscopy, when shot-to-shot beam's angular fluctuations are comparable or larger than the angular divergence of the beam itself. The slit width and the dispersion of the dipole magnet at the detection plane determine spectral energy resolution which was $\pm 15 \text{ MeV}$ for 150 MeV electrons and $\pm 50 \text{ MeV}$ for 350 MeV electrons.

High-energy quasimonoenergetic electron beams were generated using background plasma densities in the range $1.5 \times 10^{19} \leq n_e \leq 3.5 \times 10^{19} \text{ cm}^{-3}$. For most laser shots in this density range only one or two monoenergetic peaks in the spectrum were observed (inset of Fig. 4). For densities above $2.5 \times 10^{19} \text{ cm}^{-3}$ the monoenergetic peaks were superimposed on a wider electron distribution. Densities above $3.5 \times 10^{19} \text{ cm}^{-3}$ produced only broad spectral distribution. We found that the energy of the monoenergetic peak can be consistently controlled by adjusting the backing pressure of the gas jet (Fig. 4). For example, the monoenergetic peak energy increases from $80 \pm 20 \text{ MeV}$ to $120 \pm 30 \text{ MeV}$ by lowering

the plasma density from $n_e = 3.5 \times 10^{19}$ to $2 \times 10^{19} \text{ cm}^{-3}$. When the electron density is slightly below $2 \times 10^{19} \text{ cm}^{-3}$ we observed a strong increase in the peak electron energy to $\sim 250 \pm 50 \text{ MeV}$ with a highest measured energy of $320 \pm 50 \text{ MeV}$ (inset Fig. 4).^{27,37}

The scaling of electron energy gain in the entire density region can be approximated as $\Delta\mathcal{E}(\text{MeV}) = 320/n_e$, where n_e in units of 10^{19} cm^{-3} or $\Delta\mathcal{E} \approx 2m_e c^2 a_0 n_c / n_e$, where n_c is the plasma critical density. This scaling is in reasonable agreement with scaling in Ref. 24. The experimental scaling is consistent with the dephasing of relativistic electrons from the plasma wave and their slippage into the deceleration phase for plasma length greater than the dephasing length $L_{\text{dph}} \approx \lambda_p^3 / \lambda_0^2 \propto n_e^{-3/2}$.^{1,36} The energy gain acquired by electrons in the plasma wave in the mildly nonlinear regime ($a_0 \sim 1$) can be estimated as $\Delta\mathcal{E} \approx eE_{\text{wf}}L_{\text{dph}}$, where $E_{\text{wf}} \propto \sqrt{n_e}(\text{cm}^{-3})$ (V/cm) is the plasma wave amplitude, providing inverse proportional dependence of the energy gain $\Delta\mathcal{E} \propto 1/n_e$. The observed electron energy scaling as a function of plasma density demonstrate the advantage of using lower plasma densities to achieve the highest energy from the laser-wakefield structures and to produce electron beams with improved emittance and more stable angular characteristics. The drawback is that, for this case, the number of accelerated electrons is significantly reduced.

The estimate of the electron energy gain gives $\Delta\mathcal{E} = 320 \text{ MeV}$ for $n_e = 1.5 \times 10^{19} \text{ cm}^{-3}$ and $\Delta\mathcal{E} = 150 \text{ MeV}$ for $n_e = 3.5 \times 10^{19} \text{ cm}^{-3}$ in quantitative agreement with the values of maximum electron energy observed in the experiment. The corresponding wakefield amplitudes are $E_{\text{wf}} = 0.32 \text{ GV/cm}$ and $E_{\text{wf}} = 0.56 \text{ GV/cm}$. The total charge of the electron beam is determined by the number of electrons trapped in the plasma wave. Electron trapping is more efficient when the amplitude of the plasma wave is high and when the wake velocity is lower, which is the case realized at higher plasma densities. In our experiments the minimum measured electron beam divergence of 10 mrad matches the angular size of the plasma accelerating structure $\theta \sim d_0/L_{\text{pl}}$ (d_0 is the laser spot size). Higher plasma densities yield plasma waves with stronger nonlinearities and smaller radius of curvature of the wakefield structures.^{21,25,31} Acceleration in such structures is essentially a 3D process²⁶ and may lead to larger electron beam divergence and angular fluctuations.

C. Photonuclear reaction with monoenergetic electron beams

Energetic electron beams have an array of applications in radiography, radioisotope production, nuclear physics, and possibly the transmutation of nuclear waste. In particular, the multi-MeV bremsstrahlung produced using the incident electrons upon a high Z converter is an effective technique to induce photo-fission and may have additional applications in dynamic γ -ray radiography and nuclear resonance fluorescence to detect explosives or other materials.

Activation of nuclei by γ -induced reactions requires γ -ray energies corresponding to the giant resonances of the nuclei, which typically lie in the 10–20 MeV energy range for (γ, n) reactions and 5–10 MeV for $(\gamma, \text{fission})$ reactions.

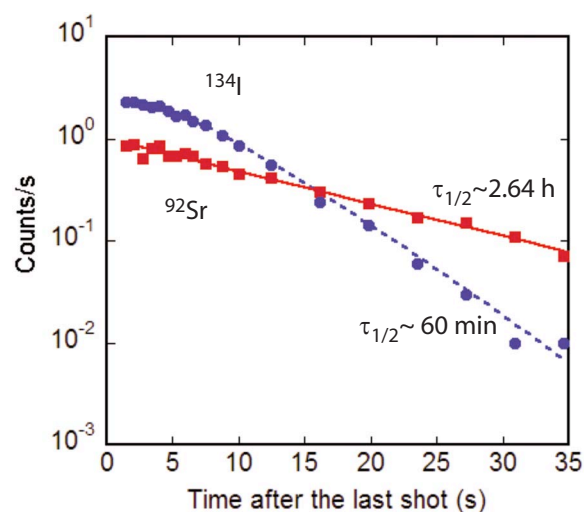


FIG. 5. (Color online) Measured count rates for the 847 keV and 1384 keV γ -rays detected, as a function of time after the last laser shot for the corresponding reactions $^{238}\text{U}(\gamma, \text{fission})^{134}\text{I}$ (\bullet) and $^{238}\text{U}(\gamma, \text{fission})^{92}\text{Sr}$ (\blacksquare). Dashed curve corresponds to the best fit to the feeding model of the ^{134}SI population through the decay of other ^{238}U fission fragment pathways. Solid line is a fit for a standard exponential decay of ^{92}Sr with half-life of 2.64 h.

Previous electron acceleration experiments with high intensity lasers interacting with gas³⁸ or solid^{39–41} targets used electron bunches with Maxwellian distributions, in the low-MeV energy range to induce nuclear activation. However, generation of γ -rays lying within the giant resonance energy range can be made significantly more efficient with a high energy monoenergetic electron source.

We optimized the electron beam's spatial profile and total charge, and consistently produced a quasimonoenergetic electron beam with a peak energy ranging between 100 and 150 MeV by adjusting plasma background density. After characterizing the electron beam and establishing its reproducibility, a 2.9 mm thick, 11 mm diameter natural uranium target was placed 15 cm behind the gas jet, where the electron beam was $\sim 3 \text{ mm}$ in diameter. Bremsstrahlung yield scales as the atomic number squared (Z^2); thus the uranium target was used both as a converter and as a fissionable target.

The uranium fission process produces, among other fission fragments, ^{134}I and ^{92}Sr with 53 min and 2.7 h half-lives, respectively. The laser was fired 72 times over $\sim 75 \text{ min}$, corresponding to roughly 1.5 ^{134}I half-lives, and an additional 18 min delay was experienced between removing the sample and the counting process. The emitted γ spectrum was recorded every 10 min for the first 1.5 h, every 20 min for the next hour, and finally every 60 min for the next 7 h. The ^{134}I and ^{92}Sr fission products were identified, using an ORTEC GAMMX Ge(Li) γ -ray detector, through their signature γ decays of 0.847 and 1.384 MeV γ rays. The presence and populations of ^{134}I and ^{92}Sr were confirmed by measuring the numbers of the emitted γ rays (background subtracted) as functions of time, as shown in Fig. 5. Primary fission to the ^{134}I fragment accounts for about one-third of the integrated total reactions. Feeding of the ^{134}I population through the decays of other ^{238}U fission fragment pathways

causes the deviation observed during the first 2 h of the measured ^{134}I decay. The secondary fission fragment pathways decaying to ^{92}Sr have shorter and decayed during the 18 min delay before counting began, thus showing little deviation from the single exponential decay model. By fitting the data after several expected lifetimes, 1.0 h and 2.64 h half-lives were determined for ^{134}I and ^{92}Sr , respectively, in relatively good agreement with the literature values of 53 min and 2.7 h.

To derive the fission yields the tabulated lifetimes and relative fission fractions for fragments contributing to ^{134}I (and ^{92}Sr) were used. The apparent total ^{134}I and ^{92}Sr isotope production yields after the last laser pulse derived from fitting the data with this model are 1.5×10^7 and 1.0×10^7 , respectively. Dividing the totals by the appropriate effective number of laser shots, and taking into account the decays between shots, gives a resultant total average fission yield of 3.3×10^5 fissions per laser shot for both the ^{134}I and ^{92}Sr data sets, which is more than an order of magnitude greater than previously achieved.

D. Electron acceleration with 70 TW laser pulses

We performed initial experiments on electron acceleration with ~ 70 TW laser pulses. The laser power increase was due to the laser pulse energy gain in an additional Ti:sapphire amplifier. The laser pulse was compressed to 30 fs in a vacuum compressor chamber equipped with 4 gratings. The output beam with diameter of ~ 10 cm was focused using $f=1.5$ m parabola to a spot size $\sim 30 \mu\text{m}$ (FWHM), ~ 2 mm above a supersonic 1.8 mm He gas jet tilted by 30° , providing a peak intensity of $\sim 6 \times 10^{18} \text{ W/cm}^2$. This intensity was approximately 1.5 times lower than the peak intensity in the experiments described in Sec. II due to some beam astigmatism. The tilting of the gas jet allowed for plasma density tapering which resulted in a down density ramp. If the density ramp and the plasma length are adjusted properly it may allow for the injection of particles at higher densities through wavebreaking and their acceleration for a longer distance in a less dense plasma region by avoiding dephasing. We used the transverse interferometry to infer the electron density distribution. For example, for a backing pressure of 10 psi the density distribution shows a $\sim 500 \mu\text{m}$ density up-ramp where the intense laser beam enters the plasma. The peak of the electron density is $1.5 \times 10^{19} \text{ cm}^{-3}$ with a long ~ 2.5 mm density down-ramp. By adjusting the backing pressure of the nozzle we vary the peak of the electron density.

Spectroscopy of the electron beams was performed using a sector magnet with the angle of 60° , magnetic field of 0.56 T and with the length along the laser axis of 13 cm. The LANEX screen was used as a detector and imaged to a CCD. A sector magnet allows for a better linearity of the dispersion compare to the dipole magnet. The setup provides energy resolution of ± 5 MeV for 100 MeV electrons, ± 17 MeV for 200 MeV and ± 35 MeV for 300 MeV. We found that electrons with energy above 100 MeV can be systematically produced for the peak electron densities between $1.6 \times 10^{19} \text{ cm}^{-3}$ and $6 \times 10^{18} \text{ cm}^{-3}$. For densities of

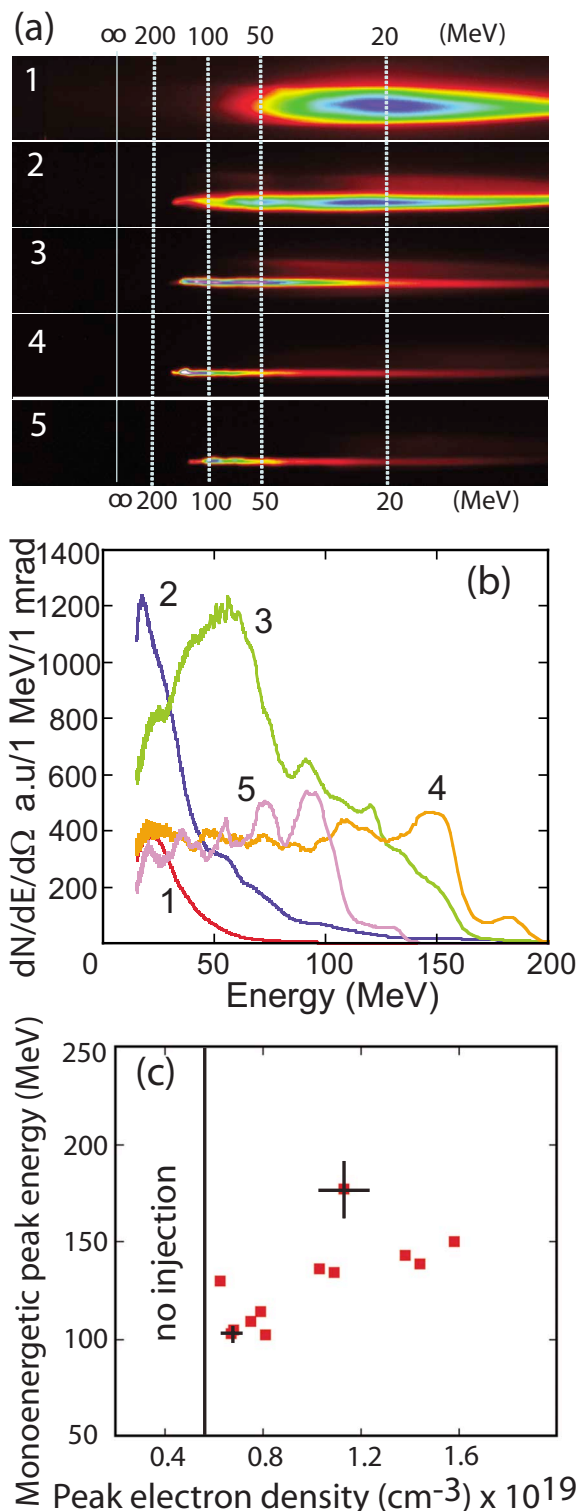


FIG. 6. (Color online) (a) Raw images of high energy electron spectra for the interaction of ~ 70 TW pulses with tilted gas jet for a peak electron density of: Panel 1, $2.3 \times 10^{19} \text{ cm}^{-3}$; panel 2, $1.7 \times 10^{19} \text{ cm}^{-3}$; panel 3, $1.5 \times 10^{19} \text{ cm}^{-3}$; panel 4, $1.1 \times 10^{19} \text{ cm}^{-3}$; and panel 5, $7.5 \times 10^{18} \text{ cm}^{-3}$. (b) The corresponding line-outs in units of $dN/dE/d\Omega$. (c) The dependence of the highest monoenergetic peak electron energy vs peak electron density (■). Crosses represent the error bars.

$1.7 \times 10^{19} \text{ cm}^{-3}$ and above electron beams with monoenergetic peak at 20 MeV were observed [spectra 1 and 2 on Fig. 6(a)]. For peak densities in the range $6 \times 10^{18} \text{ cm}^{-3} \leq n_e^{\text{peak}} \leq 1.6 \times 10^{19} \text{ cm}^{-3}$ electron beams with a divergence of only

5 mrad (FWHM) and clearly pronounced monoenergetic features were detected [spectra 3, 4, and 5 in Fig. 6(a) and corresponding line-outs in Fig. 6(b)]. The highest energy observed in the present experiments was 182 ± 15 MeV. Overall, there was a ~ 1.5 times decrease in a monoenergetic peak energy of the electron beam with the decrease of plasma density in the above range (Fig. 6(c)). Such behavior is consistent with a wakefield amplitude dependence $E_{\text{wf}} \propto \sqrt{n_e}$ (and hence electron energy gain) on plasma density and for the dephasing lengths longer than the plasma length, that was satisfied in present experiment. This work also demonstrates that for higher laser powers the plasma wavebreaking occurs at lower densities supporting Ref. 24. If the trend of decreasing the plasma wavebreaking threshold while increasing the laser power is maintained the following experiments on Hercules at ~ 200 TW power level may produce high quality electron bunches with multihundreds MeV or even GeV energies for longer interaction distances.²⁴

III. CONCLUSIONS

An optical diagnostic of laser wakefields and detailed optimization study of accelerated electron beams have been performed at the HERCULES facility in a broad range of laser and plasma parameters. At plasma densities below 10^{19} cm^{-3} the self-trapping of background electrons was negligible (no fast electrons were detected). In these regimes, transverse and longitudinal structure of the nonbroken mildly nonlinear laser wake was recorded and processed in real time in a single laser shot by using the frequency-domain holography (FDH). The wake morphology from the holographic “snapshots” agreed perfectly with the simulations by the PIC code WAKE. The presented results open a window into the microscopic physics of relativistic laser-plasma interactions. These holographic “snapshots” capture the variation in shape of the plasma wave with distance behind the driver and are essential step towards controlling electron beam properties in prospective high-power experiments. The FDH is being currently extended to higher density plasmas where the transverse wave breaking leads to self-injection of electrons in plasma waves.

For electron densities above 10^{19} cm^{-3} high-energy highly collimated quasimonoenergetic electron beams were produced with the 40 TW laser pulse. The peak electron energy could be controlled from 80 to 120 MeV by reducing the electron density from 3.5×10^{19} to $2 \times 10^{19} \text{ cm}^{-3}$. Further decrease in density from 1.8×10^{19} to $1.5 \times 10^{19} \text{ cm}^{-3}$ leads to the highest electron energies (up to 320 MeV) and the most stable electron beams. We found that the electron beam shot-to-shot angular stability was not correlated with the stability of the laser beam whose variations were only $50 \mu\text{rad}$. The characteristic scaling of the electron beam energy was consistent with dephasing of the electrons from the plasma wave. The generated high-energy quasimonoenergetic electron beams have been shown to be effective in producing the multi-MeV bremsstrahlung photons that are necessary to efficiently induce photonuclear fission in uranium. Analysis of the measured delayed γ -emission demonstrates production of

greater than 3×10^5 fission events per Joule of laser energy, which is more than an order of magnitude greater than was previously achieved.

ACKNOWLEDGMENTS

This work was supported by the National Science Foundation through the Physics Frontier Center FOCUS (Grant No. PHY-0114336). Partial support from the U.S. Department of Energy is acknowledged by S.K. and G.S. (Grant Nos. DE-FG02-04ER54763, DE-FG02-04ER41321, and DE-FG02-07ER54945) and M.D. (Grant Nos. DE-FG03-96ER0954 and DE-FG02-07ER54945). R.B., D.R.S., D.W.S., and C.R.V. were partially sponsored by the Laboratory Directed Research and Development Program of Oak Ridge National Laboratory (ORNL), managed by UT-Battelle, LLC for the U.S. Department of Energy under Contract No. DE-AC05-00OR22725.

- ¹T. Tajima and J. M. Dawson, *Phys. Rev. Lett.* **43**, 267 (1979).
- ²A. Modena, Z. Najmudin, A. E. Dangor, C. E. Clayton, K. A. Marsh, C. Joshi, V. Malka, C. B. Darrow, C. Danson, D. Neely, and F. N. Walsh, *Nature (London)* **337**, 606 (1995).
- ³K. Nakajima, D. Fisher, H. Nakanishi, Y. Kato, Y. Kitagawa, R. Kodama, K. Mima, H. Shiraga, K. Suzuki, K. Yamakawa, Y. Sakawa, T. Shoji, Y. Nishida, N. Yugami, M. Downer, and T. Tajima, *Phys. Rev. Lett.* **74**, 4428 (1995).
- ⁴D. Umstadter, S.-Y. Chen, A. Maksimchuk, G. Mourou, and R. Wagner, *Science* **273**, 472 (1996).
- ⁵V. Malka, S. Fritzler, E. Lefebvre, M.-M. Aeonard, F. Burgy, J. P. Chambaret, J.-F. Chemin, K. Krushelnick, G. Malka, S. P. D. Mangles, Z. Najmudin, M. Pittman, J.-P. Rousseau, J.-N. Scheurer, B. Walton, and A. E. Dangor, *Science* **298**, 1600 (2002).
- ⁶J. Faure, Y. Glinec, A. Pukhov, S. Kiselev, S. Gordienko, E. Lefebvre, J.-P. Rousseau, F. Burgy, and V. Malka, *Nature (London)* **431**, 541 (2004).
- ⁷C. G. R. Geddes, Cs. Toth, J. Van Tilborg, E. Esarey, C. B. Schroeder, D. Bruhwiler, C. Nieter, J. Cary, and W. P. Leemans, *Nature (London)* **431**, 538 (2004).
- ⁸S. P. D. Mangles, Z. Najmudin, A. G. R. Thomas, J. L. Collier, A. E. Dangor, E. J. Divall, P. S. Foster, J. G. Gallacher, C. J. Hooker, D. A. Jaroszynski, A. J. Langley, W. B. Mori, P. A. Norreys, F. S. Tsung, R. Viskup, B. R. Walton, and K. Krushelnick, *Nature (London)* **431**, 535 (2004).
- ⁹E. Miura, K. Koyama, S. Kato, N. Saito, M. Adachi, Y. Kawada, T. Nakamura, and M. Tanimoto, *Appl. Phys. Lett.* **86**, 251501 (2005).
- ¹⁰B. Hidding, K.-U. Amthor, B. Liesfeld, H. Schwoerer, S. Karsch, M. Geissler, L. Veisz, K. Schmid, J. G. Gallacher, S. P. Jamison, D. Jaroszynski, G. Pretzler, and R. Sauerbrey, *Phys. Rev. Lett.* **96**, 105004 (2006).
- ¹¹S. P. D. Mangles, A. G. R. Thomas, M. C. Kaluza, O. Lundh, F. Lindau, A. Persson, F. S. Tsung, Z. Najmudin, W. B. Mori, C.-G. Wahlstrom, and K. Krushelnick, *Phys. Rev. Lett.* **96**, 215001 (2006).
- ¹²J. Faure, Y. Glinec, J. J. Santos, F. Ewald, J.-P. Rousseau, S. Kiselev, A. Pukhov, T. Hosokai, and V. Malka, *Phys. Rev. Lett.* **95**, 205003 (2005).
- ¹³W. P. Leemans, B. Nagler, A. J. Gonsalves, Cs. Toth, K. Nakamura, C. G. R. Geddes, E. Esarey, C. B. Schroeder, and S. M. Hooker, *Nat. Phys.* **2**, 696 (2006).
- ¹⁴J. Faure, C. Rechatin, A. Norlin, A. Lifschitz, Y. Glinec, and V. Malka, *Nature (London)* **444**, 737 (2006).
- ¹⁵C. W. Siders, S. P. Le Blanc, D. Fisher, T. Tajima, M. C. Downer, A. Babine, A. Stepanov, and A. Sergeev, *Phys. Rev. Lett.* **76**, 3570 (1996).
- ¹⁶J. R. Marques, F. Dorchies, F. Amiranoff, P. Audebert, J. C. Gauthier, J. P. Geindre, A. Antonetti, T. M. Antonsen, P. Chessa, and P. Mora, *Phys. Plasmas* **10**, 1124 (1998).
- ¹⁷E. Takahashi, H. Honda, E. Miura, N. Yugami, Y. Nishida, K. Katsura, and K. Kondo, *Phys. Rev. E* **62**, 7247 (2000).
- ¹⁸H. Kotaki, M. Kando, T. Oketa, S. Masuda, J. K. Koga, S. Kondo, S. Kanazawa, T. Yokoyama, T. Matoba, and K. Nakajima, *Phys. Plasmas* **9**, 1392 (2002).
- ¹⁹J. P. Geindre, P. Audebert, A. Rousse, F. Fallies, J. C. Gauthier, A.

- Mysyrowicz, A. Dos Santos, G. Hamoniaux, and A. Antonetti, *Opt. Lett.* **19**, 1997 (1994).
- ²⁰S. P. Le Blanc, E. W. Gaul, N. H. Matlis, A. Rundquist, and M. C. Downer, *Opt. Lett.* **25**, 764 (2000).
- ²¹N. H. Matlis, S. Reed, S. S. Bulanov, V. Chvykov, G. Kalintchenko, T. Matsuoka, P. Rousseau, V. Yanovsky, A. Maksimchuk, S. Kalmykov, G. Shvets, and M. C. Downer, *Nat. Phys.* **2**, 749 (2006).
- ²²V. Malka, J. Faure, Y. Glinec, A. Pukhov, and J.-P. Rousseau, *Phys. Plasmas* **12**, 056702 (2005).
- ²³S. Gordienko and A. Pukhov, *Phys. Plasmas* **12**, 043109 (2005).
- ²⁴W. Lu, T. Tzoufras, C. Joshi, F. S. Tsung, W. B. Mori, J. Vieira, R. A. Fonseca, and L. O. Silva, *Phys. Rev. ST Accel. Beams* **10**, 061301 (2007).
- ²⁵A. Pukhov and J. Meyer-ter-Vehn, *Appl. Phys. B* **74**, 355 (2002).
- ²⁶S. V. Bulanov, M. Yamagiwa, T. Z. Esirkepov, J. K. Koga, M. Kando, Y. Ueshima, K. Saito, and D. Wakabayashi, *Phys. Plasmas* **12**, 073103 (2005).
- ²⁷A. Maksimchuk, S. Reed, N. Naumova, V. Chvykov, B. Hou, G. Kalintchenko, T. Matsuoka, J. Nees, P. Rousseau, G. Mourou, and V. Yanovsky, *Appl. Phys. B: Lasers Opt.* **89**, 201 (2007).
- ²⁸S. A. Reed, V. Chvykov, G. Kalintchenko, T. Matsuoka, P. Rousseau, V. Yanovsky, C. R. Vane, J. R. Beene, D. Stracener, D. R. Schultz, and A. Maksimchuk, *Appl. Phys. Lett.* **89**, 231107 (2006).
- ²⁹S. A. Reed, V. Chvykov, G. Kalintchenko, T. Matsuoka, V. Yanovsky, C. R. Vane, J. R. Beene, D. Stracener, D. R. Schultz, and A. Maksimchuk, *J. Appl. Phys.* **102**, 073103 (2007).
- ³⁰S.-W. Bahk, P. Rousseau, T. A. Planchon, V. Chvykov, G. Kalintchenko, A. Maksimchuk, G. A. Mourou, and V. Yanovsky, *Opt. Lett.* **29**, 2837 (2004).
- ³¹S. V. Bulanov, F. Pegoraro, A. M. Pukhov, and A. S. Sakharov, *Phys. Rev. Lett.* **78**, 4205 (1997).
- ³²N. E. Andreev, L. M. Gorbunov, and R. R. Ramazashvili, *Plasma Phys. Rep.* **23**, 277 (1997).
- ³³D. Decker, W. B. Mori, and T. Katsouleas, *Phys. Rev. E* **50**, R3338 (1994).
- ³⁴P. Mora and T. M. Antonsen, Jr., *Phys. Plasmas* **4**, 217 (1997).
- ³⁵S. Yu. Kalmykov, L. M. Gorbunov, P. Mora, and G. Shvets, *Phys. Plasmas* **13**, 113102 (2006).
- ³⁶P. Sprangle, E. Esarey, A. Ting, and G. Joyce, *Appl. Phys. Lett.* **53**, 2146 (1988).
- ³⁷A. Maksimchuk, S. Reed, N. Naumova, V. Chvykov, B. Hou, G. Kalintchenko, T. Matsuoka, J. Nees, P. Rousseau, G. Mourou, and V. Yanovsky, *J. Phys. IV* **133**, 1123 (2006).
- ³⁸W. P. Leemans, D. Rodgers, P. E. Catravas, C. G. R. Geddes, G. Fubiani, E. Esarey, B. A. Shadwick, R. Donahue, and A. Smith, *Phys. Plasmas* **8**, 2510 (2001).
- ³⁹H. Schwoerer, P. Gibbon, S. Duesterer, R. Brehens, C. Ziener, C. Reich, and R. Sauerbrey, *Phys. Rev. Lett.* **86**, 2317 (2001).
- ⁴⁰G. Malka, M. M. Aleanard, J. F. Chemin, G. Claverie, M. R. Harston, V. Tikhonchuk, J. N. Scheurer, S. Fritzler, V. Malka, P. Balcou, G. Grillon, S. Moustazis, L. Notebaert, M. Pittman, and E. Lefebvre, *Proc. SPIE* **4510**, 47 (2001).
- ⁴¹B. Liesfeld, K.-U. Amthor, F. Ewald, H. Schwoerer, J. Magill, J. Galy, G. Lander, and R. Sauerbrey, *Appl. Phys. B: Lasers Opt.* **B79**, 1047 (2004).